

## FIRT: Filtered iterative reconstruction technique with information restoration



Yu Chen <sup>a,c,1</sup>, Yan Zhang <sup>b,1</sup>, Kai Zhang <sup>b,c,\*1</sup>, Yuchen Deng <sup>b,c</sup>, Shengliu Wang <sup>b,c</sup>, Fa Zhang <sup>a,\*</sup>, Fei Sun <sup>b,c,d,\*</sup>

<sup>a</sup> Key Lab of Intelligent Information Processing, Institute of Computing Technology, Chinese Academy of Sciences, Beijing 100190, China

<sup>b</sup> National Laboratory of Biomacromolecules, Institute of Biophysics, Chinese Academy of Sciences, 15 Datun Road, Beijing 100101, China

<sup>c</sup> University of Chinese Academy of Sciences, Beijing, China

<sup>d</sup> Center for Biological Imaging, Institute of Biophysics, Chinese Academy of Sciences, 15 Datun Road, Beijing 100101, China

### ARTICLE INFO

#### Article history:

Received 21 December 2015

Received in revised form 27 April 2016

Accepted 28 April 2016

Available online 29 April 2016

#### Keywords:

Algebra reconstruction technique

Electron tomography

Filtered iterative reconstruction technique

Information restoration

Nonlinear diffusion filter

### ABSTRACT

Electron tomography (ET) combining subsequent sub-volume averaging has been becoming a unique way to study the *in situ* 3D structures of macromolecular complexes. However, information missing in electron tomography due to limited angular sampling is still the bottleneck in high-resolution electron tomography application. Here, based on the understanding of smooth nature of biological specimen, we present a new iterative image reconstruction algorithm, FIRT (filtered iterative reconstruction technique) for electron tomography by combining the algebra reconstruction technique (ART) and the nonlinear diffusion (ND) filter technique. Using both simulated and experimental data, in comparison to ART and weight back projection method, we proved that FIRT could generate a better reconstruction with reduced ray artifacts and significant improved correlation with the ground truth and partially restore the information at the non-sampled angular region, which was proved by investigating the 90° re-projection and by the cross-validation method. This new algorithm will be subsequently useful in the future for both cellular and molecular ET with better quality and improved structural details.

© 2016 The Authors. Published by Elsevier Inc. This is an open access article under the CC BY-NC-ND license (<http://creativecommons.org/licenses/by-nc-nd/4.0/>).

## 1. Introduction

Electron tomography (ET) is an important method for studying the cell ultrastructure in three-dimensional space (Fridman et al., 2012; Lucic et al., 2013; Rigort et al., 2012; Yahav et al., 2011) and investigating *in situ* structures and conformational dynamics of macromolecular complexes through a sub-volume averaging approach (Castano-Diez et al., 2012). Recent advancements in instrumentation (e.g., phase plates), the experimental workflow, and image processing (Asano et al., 2015; Engel et al., 2015; Schur et al., 2015) have opened up new possibilities in visualizing *in situ* macromolecular structures with sub-nanometer detail.

However, current ET methods exhibit problems such as missing information, especially missing wedges, owing to the limited

angular sampling during data collection (Orlova and Saibil, 2011) because of the physical restriction of the sample stage and the specificity of the biological samples. The physical restrictions of a conventional sample holder or grid normally allow a tilt angle from -70° to 70°, and some specially designed holders permit a tilt angle of -83° to 83°. More importantly, considering the severe radiation damage caused to biological specimens by an electron beam (Frank, 2006), in reasonably high-resolution cryo-electron tomography (cryo-ET) studies, the total dose used during data collection should be minimized; normally, it is limited to less than 100 e<sup>-</sup>/Å<sup>2</sup>. In addition, the quality and resolution of the final reconstructed tomogram are closely related to the alignment accuracy of the tilt series of micrographs; this is significantly affected by the signal-to-noise ratio (SNR) of each tilting micrograph. To maintain a reasonable SNR to accurately compensate for the mechanical shift and rotation errors and to determine the defocus parameters for each tilting micrograph, the fractionated dose in each micrograph should be sufficiently high. Therefore, to balance the minimized total dose and high SNR of each tilt micrograph, the angular sampling during ET data collection should be limited; for example, tilting should be limited from -70° to 70° (or an even smaller range) with angular steps of 2°–3° (or even larger). Consequently, the regions between adjacent tilt angles and at high tilt

\* Corresponding authors at: Medical Research Council Laboratory of Molecular Biology, Division of Structural Studies, Francis Crick Avenue, Cambridge CB2 0QH, UK (K. Zhang). Institute of Computing Technology, Chinese Academy of Sciences, Beijing 100190, China (F. Zhang). Center for Biological Imaging, Institute of Biophysics, Chinese Academy of Sciences, 15 Datun Road, Beijing 100101, China (F. Sun).

E-mail addresses: [kzhang@mrc-lmb.cam.ac.uk](mailto:kzhang@mrc-lmb.cam.ac.uk) (K. Zhang), [zhangfa@ict.ac.cn](mailto:zhangfa@ict.ac.cn) (F. Zhang), [fesun@sun5.ibp.ac.cn](mailto:fesun@sun5.ibp.ac.cn) (F. Sun).

<sup>1</sup> These authors make equal contributions to this work.

angles ( $-90^\circ$  to  $-70^\circ$  and  $70$ – $90^\circ$ , also called missing wedges) are not sampled. However, the limited angular sampling induces severe ray artifacts, structural elongation, and distortion effects in the final reconstructed tomogram, thus limiting the reconstruction resolution, eliminating structural details, and becoming a bottleneck for the subsequent interpretation and processing.

Many algorithms have been developed for reconstructing tomograms from ET data and improving the reconstruction quality. These algorithms include Fourier reconstruction, back projection (Sahiner and Yagle, 1993), weighted back projection (WBP) (Radermacher, 1992), the algebra reconstruction technique (ART) (Gordon et al., 1970; Kak and Slaney, 1989), the simultaneous algebra reconstruction technique (SART) (Andersen and Kak, 1984), and the simultaneous iterative reconstruction technique (SIRT) (Gilbert, 1972). Fourier reconstruction and WBP are much faster than the ART, SART, and SIRT. However, the estimation of the missing wedge information in Fourier reconstruction is inaccurate and unreliable. WBP is the most commonly used algorithm in ET reconstruction because of its high performance in both computational speed and preservation of structural details; however, it may cause several artifacts when the data set is very noisy or the angular step becomes large. The ART, SART, and SIRT are iterative algebra methods that perform reconstruction in real space. They normally overfit the noise during iterations and enhance the low-frequency information with good contrast; however, they lose the high-frequency information. In general, none of these traditional methods can prevent the artifacts induced by incomplete angular sampling during ET data collection.

Several trials have been conducted to address the missing information problem in recent years. Song et al. (2012) proposed a method that involves directly removing the high-contrast area in cryo-ET tomograms to reduce the artifacts caused by the missing wedge problem. This method focuses on artifact compensation and does not recover any missing information. An alternative approach is dual-axis and conical tomography (Arslan et al., 2006; Lanzavecchia et al., 2005; Mastronarde, 1997; Zampighi et al., 2005), which rotates the sample along two vertical or different tilt axes for collecting multiple tomography data. These approaches cannot prevent the radiation damage problem, and they also leave a conical area in which information cannot be measured. In addition, researchers have attempted to partially restore information within the non-sampled regions on the basis of prior knowledge of the specimen (e.g., sparseness in a proper domain) by using compressed sensing (CS) theory (Goris et al., 2012; Leary et al., 2013). However, to the best of our knowledge, this CS-based reconstruction method has been restricted to materials science applications, in which the SNR of each micrograph should be sufficiently high to keep the assumed prior knowledge reliable. The maximum a posteriori expectation maximization technique is also applied for ET reconstruction. This method yields a higher resolution and higher contrast than those of WBP (Frank, 2006) and SIRT (Paavolainen et al., 2014) with minimum restoration of information; however, this method has not yet been validated adequately.

In addition to developing novel reconstruction algorithms for addressing the limited angular sampling problem in ET, researchers have also developed many postprocessing image filtering tools for reducing reconstruction artifacts, enhancing contrast, and reducing noise in the final tomogram, which is important for subsequent structural analysis and interpretation. These filtering tools include the low-pass filter, the Wiener filter, the bilateral filter, nonlinear anisotropic diffusion (NAD) (Weickert, 1998), and NAD with edge-enhanced diffusion (NAD-EED) (Frangakis and Hegerl, 2001). NAD-EED shows high performance in noise suppression and specimen morphology and edge preservation, and therefore, it has been widely used in cellular ET applications (Kremer et al., 1996).

In the present study, we introduced a filtering process for tomographic reconstruction in accordance with the following principles. Mathematically, the reconstruction of electron tomograms is a type of ill-posed inverse problem owing to the limited angular sampling condition. In theory, no unique solution is available for electron tomogram reconstruction without any prior knowledge available. Fourier interpolation reconstruction and WBP can provide one approximation of the authentic solution, whereas the iterative methods (ART, SART, and SIRT) converge to other local minima and also approximate the authentic solution. However, by introducing prior knowledge about the biological specimen, the iterations can be constrained to the global minimum (i.e., the authentic solution). The nonlinear diffusion (ND) filter (Perona and Malik, 1990) has been used to preserve both structural edges and smoothness (Frank, 2006), which constitute useful prior knowledge on most biological specimens. Thus, combining ND filtering and the iterative methods may yield a more accurate approximation of the authentic solution with missing information restored. Here, we determined an effective approach that entails combining ND and the ART to yield a new reconstruction algorithm, which we call the filtered iterative reconstruction technique (FIRT).

The FIRT enables 3D reconstruction in real space by using the ART and corrects the reconstruction in each iterative cycle by using the ND filter. This correction can prevent the ART from converging to a local minimum. Tests on both simulated and experimental data sets for a biological specimen including a negatively stained protein complex and a resin-embedded cell section proved that the FIRT could significantly improve the reconstruction quality with reduced ray artifacts and partial restoration of missing information in the non-sampled angular region.

## 2. Theory and methods

### 2.1. Nonlinear diffusion (ND)

Diffusion is a physical process that equilibrates differences in heat or concentration of matter. In the field of image processing, diffusion is described by a partial differential equation, where the pixel value changes with a rate determined by the diffusion coefficient and its pixel value gradient in comparison to that of adjacent pixels. In general, linear diffusion with a constant diffusion coefficient is mathematically equivalent to Gaussian low-pass filtering; it results in a blurred and smoothed image, but it does not preserve the edge information in the image. To preserve the edge during noise reduction, Perona and Malik (1990) modified the linear diffusion function into the nonlinear form given by Eq. (1), which minimizes or blocks the diffusion flux across edges.

$$I^{t+1} = I^t + \tau \cdot \frac{\nabla I}{1 + (\frac{\nabla I}{K})^2} \quad (1)$$

Here,  $I$  is the image,  $t$  is the iterative number (i.e., the diffusion time),  $\tau$  is a constant coefficient for keeping the overall diffusion stable and  $0 < \tau \leq 1/4$  (in the present study,  $\tau = 0.2$ ),  $\nabla$  is the gradient operator, and  $K$  is the threshold value for controlling the diffusion intensity, which varies according to the features of different images to maintain the edge information. The implementation of ND in this study is described in detail by using pseudo codes in Appendix A.

### 2.2. Algebra reconstruction technique (ART)

The ET reconstruction problem can be defined as follows. Given a collection of 2D projection images  $P$ , the 3D structure  $S$  that produces these projection images is determined. The dimension of the

projection data is usually far lesser than that of the 3D structure owing to the limited angular sampling, yielding an ill-posed mathematical problem. This type of ill-posed problem can be formulated as a large linear equation system  $P = AS + N$ , where  $A$  is the projection matrix,  $S$  and  $P$  are the 3D volume and 2D projections, respectively, and  $N$  is the noise introduced during data collection. The ART (Gordon et al., 1970; Kak and Slaney, 1989) is an algebraic algorithm that is designed to solve this underdetermined problem. It attempts to iteratively approximate  $S$  through discretization, and this can be expressed as a linear combination of some fixed basis functions (e.g., voxels):

$$S_i^{k+1} = S_i^k + \gamma \cdot \frac{P_r - P_r^k}{\sum_{j=1}^V w_{r,j}^2} w_{r,i}, \quad r = 1, 2, \dots, R. \quad (2)$$

$$P_r^k = \sum_{j=1}^V w_{r,j} \cdot S_j^k \quad (3)$$

where  $k$  is the iteration number;  $S^k$  denotes the  $k^{\text{th}}$  iteration results of the 3D structure  $S$ ;  $i$  is the index of the voxel of  $S$  or  $S^k$ ;  $S_j^k$  is the  $j^{\text{th}}$  voxel of  $S^k$ ;  $V$  is the total number of voxels of  $S$  or  $S^k$ ;  $P_r$  corresponds to the pixel value of the projection image at the cross point of the  $r$ th projection ray;  $P_r^k$  is the calculated re-projection of  $S^k$  at the  $r$ th projection ray;  $w_{r,i}$  is the weight of the voxel  $S_i$  that contributes to the  $r$ th projection ray, which is determined by the bilinear interpolation method in this study; and  $R$  is the total number of projection rays. Here, we define one ART iteration cycle as a cycle in which all  $R$  projection rays have just been used (each ray is used one time) to update  $S^k$ . The implementation of the ART in this study is described in detail by using pseudo codes in Appendix B.

### 2.3. Filtered iterative reconstruction technique (FIRT)

The ART solves the 3D reconstruction problem as a linear equation array problem through an iterative approach without using any prior knowledge. The smoothness of biological structures has been successfully applied as a type of prior knowledge in recent single-particle analyses with improved map quality (Scheres, 2012a,b). In this study, we aimed to introduce both the smoothness and the edge preservation of the biological specimen as prior knowledge into the ART iteration and thereby improve the ART reconstruction quality. The designed algorithm combines the ART and ND filtering and thus is called the FIRT.

First, an initial tomogram is generated from an unfiltered aligned tilt series of projections. A specially designed ND filter is then used to denoise the 3D tomogram and reduce the ray artifacts. Subsequently, the denoised 3D volume is reused as a starting model for another ART iteration cycle. Repeating these procedures for several rounds yields the final result.

The algorithm and workflow of the FIRT (Fig. 1) are described as follows.

**Step 1.** Initialize  $S^0$  to be zero.

**Step 2.** Using  $S^k$  as the initial value, apply the traditional ART with one iteration cycle to generate  $S_{\text{art}}^k$ .

If  $k = K$ , then  $S = S_{\text{art}}^k$ ; therefore, perform step 4. Otherwise, perform step 3.

Here,  $K$  is a user-defined parameter that represents the total number of iterations for the FIRT.

**Step 3.** Apply the ND filter to  $S_{\text{art}}^k$  to generate  $S^{k+1}$ . Then, perform step 2.

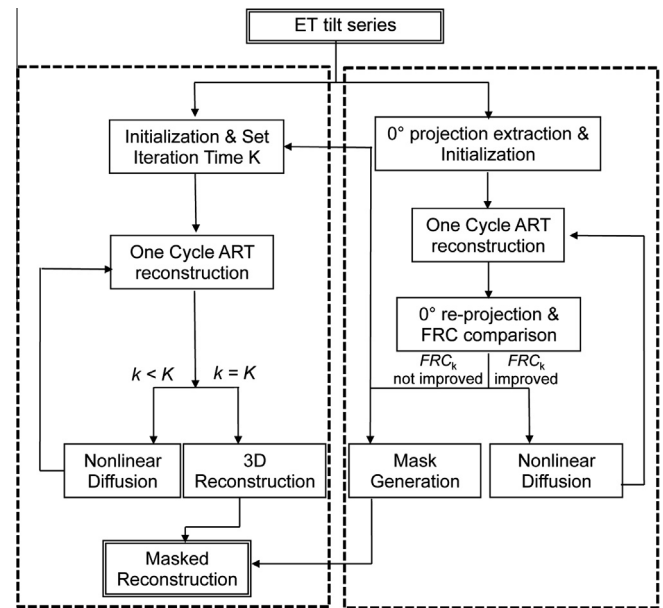


**Fig. 1.** The schematic workflow of the FIRT algorithm. The left part in the dashed box represents the complete FIRT iteration. The right part is called omit FIRT-reconstruction and used to monitor the convergence of FIRT iteration, avoid overfitting to the noise. The right part also determines a mask in Fourier domain, which will be used in the left part.

During this step, we segment  $S_{\text{art}}^k$  slices (XZ-plane, which is also the ART reconstruction plane) and apply two-dimensional ND filtering to these slices.

**Step 4.** Apply a mask (see Fig. 2) to  $S$  (generated from step 2) in the Fourier space to generate the final reconstruction tomogram  $S_{\text{mask}}$ .

Over-filtering by the ND or using improper diffusion parameters causes piecewise effects and smoothes some structural details. This is equivalent to filling the unsampled areas (missing wedge and gaps between sampled angles) in the Fourier space with incorrect information. To avoid these piecewise artifacts in real space and ensure that we fill information in the unsampled areas as accurately as possible for the FIRT, we masked  $S$  in the Fourier space to keep all the sampled areas and low-frequency areas (Fig. 2). The radius of the low-frequency areas could be determined according to a Fourier ring correlation (FRC) of 0.5 in cross-validation, as described in the following section. The masked volume  $S_{\text{mask}}$  is the final result obtained by the FIRT.

### 2.4. Cross-validation procedure for the FIRT

During subsequent experiments, we found that the FIRT could effectively restore some information in the non-sampled angular region. Thus, to evaluate the restored information, we used a cross-validation technique (see Fig. 1) similar to the resolution criterion method (Cardone et al., 2005) to evaluate the authenticity of information restoration. This cross-validation method can also be used to determine the total iteration number  $K$  and the radius of the mask used to filter out the inaccurately restored information, as described in the previous section.

**Step 1.** Extract the minimum tilt projection (normally the 0° projection) from the whole aligned tilt data set. This projection is not involved in the following cross-validation process and is used as a type of “ground truth” to perform the cross-validation.

**Step 2.** Initialize  $S^0$  to zero.

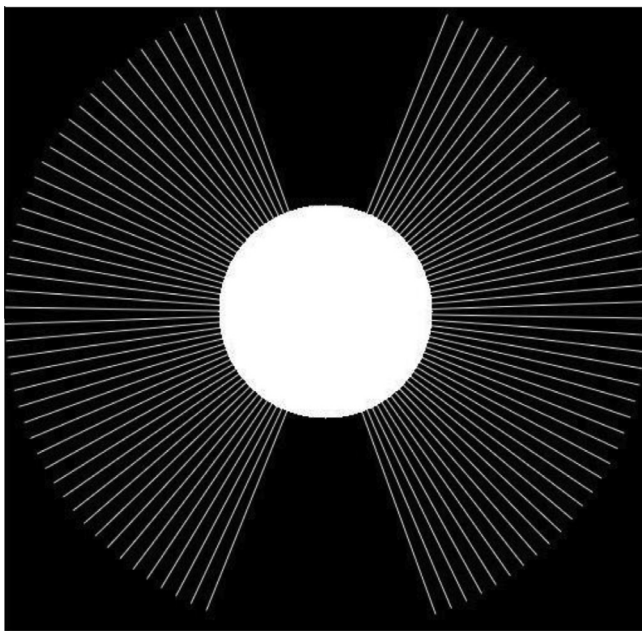


**Fig. 2.** The schematic diagram of the filtering mask in Fourier domain. The disk radius is determined by FRC-0.5 criterion from the cross validation procedure. The black area is masking out for filtering. The white rays represent the sampled tilts.

**Step 3.** Using  $S^k$  as the initial value, apply the traditional ART to generate  $S_{art}^k$ . Subsequently,  $S_{art}^k$  is reprojected along the extracted tilt direction. The FRC is calculated between the reprojection and the ground truth, and it is denoted as  $FRC_k$ . If  $FRC_k$  is not improved in comparison to  $FRC_{k-1}$ , the total iteration number of the FIRT is determined as  $K = k$  and the radius corresponding to an  $FRC_k$  of 0.5 is used as the radius of the mask. Otherwise, perform Step 4.

**Step 4.** Apply the ND filter to  $S_{art}^k$  to generate  $S^{k+1}$  and then perform step 3.

Cross-validation is used to evaluate the reconstruction results; furthermore, it provides information about the extent to which the recovered information is reliable. To suppress the filling potential error in the unsampled areas, we keep only recovered information with an FRC in cross-validation greater than 0.5, where it is reliable statistically.

The FIRT was implemented as a standalone program by using the C programming language, and it can be run in parallel by using the message passing interface. Version 1.0 can be downloaded from the link (<http://feilab.ibp.ac.cn/LBEMSB/FIRT.html>). Table 1 summarizes the computational costs of the FIRT in comparison with those of the SIRT.

## 2.5. Generation of simulated data sets

A 3D map of the 80S ribosome was generated from its crystal structure (PDB code: 4V7H) (Taylor et al., 2009) by using

e2pdb2mrc.py in EMAN2 (Ludtke et al., 1999) with a pixel size of 1 Å. This map was then low-pass filtered to its half Nyquist frequency. Finally, a series of projections of this low-passed map were obtained by simulating the projection process in ET with sampling angles from  $-70^\circ$  to  $70^\circ$  with steps of  $1^\circ$  and  $-69^\circ$  to  $69^\circ$  with steps of  $3^\circ$ . The projection was performed using the IMOD package (Kremer et al., 1996).

Different levels of Gaussian noise were added to the simulated projection series, yielding three simulated tomographic data sets with SNRs of 1, 0.5, and 0.1. In the present study, the SNR was defined as follows:

$$\text{SNR} = \frac{\sigma_{\text{signal}}^2}{\sigma_{\text{noise}}^2} \quad (4)$$

where  $\sigma_{\text{signal}}^2$  and  $\sigma_{\text{noise}}^2$  are the variances of the signal and noise, respectively.

## 2.6. Acquisition of the experimental tomographic data set

A protein specimen of COPI, which is involved in vesicle trafficking from the Golgi complex to the endoplasmic reticulum and contains seven subunits with a molecular weight of approximately 600 kDa (Schekman and Orci, 1996), was negatively stained with uranyl acetate on an ultrathin carbon film coated copper grid, which was pre-coated with 10-nm gold particles. The tomographic tilt series of this negatively stained sample was recorded using the Ceta CMOS camera (FEI, Netherlands), which is equipped with a 200-kV Talos F200C transmission electron microscope (FEI, Netherlands) under normal magnification of 57,000. The final pixel size of the micrograph was 1.81 Å. The sampling angles ranged from  $-60^\circ$  to  $60^\circ$  with steps of  $1^\circ$ , and the average radiation dose for each micrograph was  $20 \text{ e}^-/\text{\AA}^2$ . The tilt series was automatically aligned on the basis of fiducial gold markers by using MarkerAuto (Han et al., 2015).

We also tested the efficiency of the FIRT under a larger angle step with a data set of  $3^\circ$  angle increment steps. The data set was generated by extracting every three projections from the above original data set.

Another experimental data set on a resin-embedded plastic section of rat liver tissue was used to test the FIRT performance. The tilt series of this data set were recorded using an Ultrascan 1000 CCD camera (Gatan, US) equipped with a 200-kV Tecnai 20 transmission electron microscope (FEI, Netherlands). The final pixel size was 4.12 Å, and the sampling angles ranged from  $-54^\circ$  to  $57^\circ$  with increments of  $1^\circ$ . The tilt series was automatically aligned using our marker-free alignment program atom\_align (Han et al., 2014).

## 3. Results

In the following section, if not defined otherwise explicitly, ART1 is defined as one cycle of ART iteration; ART2, as two cycles of ART iteration; and so on. FIRT20 is defined as 20 cycles of FIRT iteration.

### 3.1. The ART converges quickly but is sensitive to noise

The ART achieves rapid convergence. However, it is sensitive to noise, and the reconstruction results exhibit a very noisy salt-and-pepper characteristic (Wan et al., 2011). Here, we used the simulated data sets to test the ART performance for different iteration cycles.

The simulated data sets without noise or with an SNR of 1 were reconstructed using ART1, ART20, and ART50. For comparison and control, these data sets were also reconstructed using WBP. Fourier

**Table 1**

The computational costs of FIRT in comparison with SIRT. Considering the convergence speed, we compared the computational cost of FIRT with 20 iterations (FIRT20) and the cost of SIRT with 200 iterations (SIRT200).

Size of one slice	FIRT20	SIRT200
512 × 512 (one CPU)	28 s	23 s
1024 × 1024 (one CPU)	3 min 55 s	1 min 29 s
2048 × 2048 (one CPU)	15 min 27 s	8 min 20 s

**Table 2**

The PCC and the resolution (FSC-0.5 criterion) of the reconstructions by ART for the noise-free and the SNR = 1 noisy simulated datasets (see also Fig. 3).

SNR	Method	PCC	Resolution (FSC = 0.5)
$\infty$ (noise-free)	ART 1	0.953	3.06 Å
$\infty$ (noise-free)	ART20	0.987	2.84 Å
$\infty$ (noise-free)	ART50	0.988	2.84 Å
$\infty$ (noise-free)	WBP	—	2.39 Å
1	ART 1	0.855	8.36 Å
1	ART20	0.969	9.73 Å
1	ART50	0.970	10.4 Å
1	WBP	—	8.66 Å

shell correction (FSC) curves were calculated between the reconstructions and the ground truth, and the FSC criterion of 0.5 was used to assess the reconstruction resolution. Projection cross-correlations (PCCs) between the sampled projections and the reprojections of the reconstructions were calculated to investigate the consistency between the data and the reconstructions.

The reconstruction of the noise-free data set shows that the ART yields a higher PCC as the number of iteration cycles increases (Table 2); simultaneously, the FSC curve improves (Fig. 3A and Table 2). However, the reconstruction of the data set with an SNR of 1 shows that although the PCC still increases gradually as the number of iteration cycles increases (Table 2), the FSC worsens, and ART1 shows the highest reconstruction quality, with the quality being close to that shown by WBP (Fig. 3B). These opposite behaviors of the ART between noise-free and noisy data sets suggest significant over-fitting during ART iteration, as a result of which the ART shows greater sensitivity to noise. Thus, considering the fast convergence of the ART, ART1 is sufficient to yield a satisfactory reconstruction that is close to that of WBP and to avoid noise over-fitting. In subsequent experiments and computations regarding the FIRT, the number of iteration cycles for the ART is always set as one.

### 3.2. The FIRT reduces ray artifacts and restores missing information

First, an FIRT test was performed on the noise-free simulated ribosome data set. The central XZ-slice and 90° projection (Fig. 4A) of the ground truth were generated for a subsequent comparison. It should be noted that the 90° projection is located in the non-sampled region of the simulated tomographic data set.

We calculated the reconstructions by FIRT20 as well as by ART1, ART20, and WBP for the simulation data with projection tilt angle increments of 1° and 3°, respectively (Fig. 4). We also calculated

the cross-validation FRC and the FSC curves between the reconstructed maps and the ground truth (Fig. 4B).

We generated the mask according to the cross-validation FRC of 0.5. When this mask is applied, the high-frequency areas of the FIRT FSC are superior to those of the FIRT without the mask, suggesting that the restored information at a high frequency is not correct and must be masked out. Furthermore, we found that FIRT20 yields a significantly superior map that is close to the ground truth in comparison with both the ART and WBP (Fig. 4A and B). For a larger angular increment, the improvement in the FIRT becomes more obvious (Fig. 4B). The FSC curve from ART20 was used as a control to confirm that the improvement by FIRT20 is indeed due to the introduction of ND into the ART iteration (Fig. 4B).

The ray artifacts observed in the central XZ-slices of maps reconstructed by WBP and ART1 are mostly eliminated in the map reconstructed by FIRT20 (Fig. 4A). As mentioned in the introduction, the ray artifacts are mainly caused by the incorrect estimation of missing information, which is normally replaced by zeros in most conventional reconstruction algorithms. The elimination of ray artifacts by the FIRT reminds us that the FIRT can potentially recover some missing information in the non-sampled region. To verify this, we calculated the Fourier transform of the reconstructed maps and compared their central XZ-slices. In consistency with our prediction, the FIRT recovers much information not only in the missing wedge but also in the non-sampled interval regions, which are filled mostly by zeros in the WBP and ART reconstructions (Fig. 4C).

To validate the information recovered by the FIRT, especially the information at the missing wedge, we calculated the reprojectations of these reconstructed maps at 90°, where sampling is impossible during tomographic data collection. In comparison to the 90° projection of the ground truth (Fig. 4A), the reprojeciton from WBP reconstruction does not provide any recognized information with an elongated shape; the reprojeciton from ART reconstruction can suggest only an overall recognized shape without any details; and the reprojeciton from FIRT reconstruction appears to be close to the ground truth (Fig. 4D).

Thus, the FIRT can provide a significantly improved reconstruction by reducing ray artifacts and restoring missing information of the specimen at the non-sampled angular regions.

### 3.3. Testing the FIRT by using noisy simulated data sets

For angle increments of 1° and 3°, respectively, the simulated tilt series of the tomographic data sets of ribosomes with SNRs of

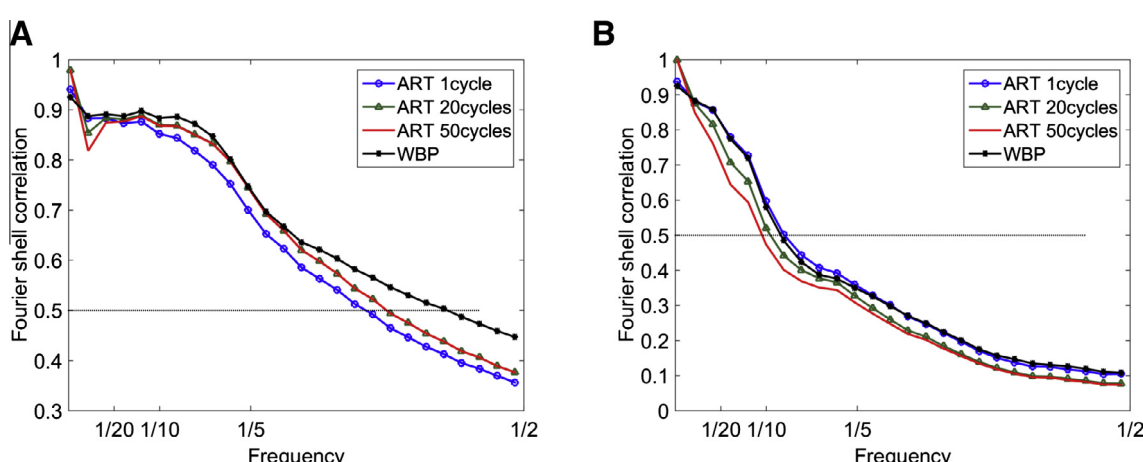


**Fig. 3.** The convergence and noise sensitivity of the ART. (A) and (B) The FSC curves between the reconstructions and the ground truth for the noise-free simulated dataset in (A) and the SNR = 1 simulated dataset in (B).

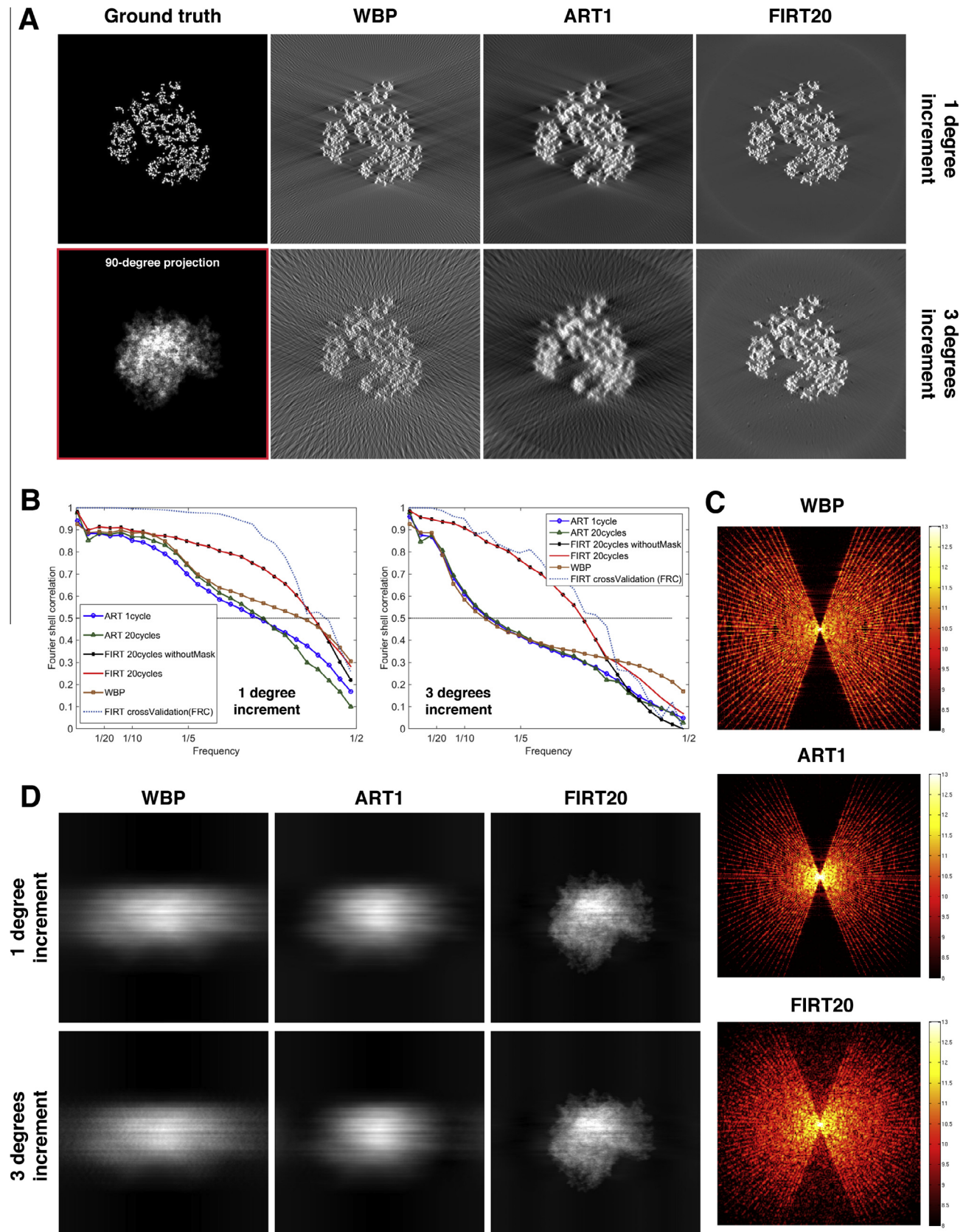


**Fig. 4.** FIRT reconstruction of noise-free simulated datasets with the angular step 1° and 3°. (A) The first column are the central XZ-slice of the ground truth (upper) and the 90° projection of the ground true map (lower) respectively; the second to fourth columns are the central XZ-slices of the reconstructions by WBP, ART1 and FIRT20 for 1° and 3° increment, respectively. (B) The cross validation FRC curves and the FSC curves between the reconstructions and the ground truth. (C) The central XZ-slices of the Fourier transformation of the corresponding reconstructions for the dataset with the angular increment of 3°. (D) The 90° re-projections of the corresponding reconstructions.

1, 0.5, and 0.1 were separately subjected to reconstruction with FIRT20 as well as ART1, ART20, and WBP. The central XZ-slices of the reconstructions (Fig. 5A) and their 90° reprojections (Fig. 5A) were computed and compared with the noise-free ground truth (Fig. 4A). In accordance with the test of the noise-free data set, for the simulated data set with an SNR of 1, the ray artifacts are still clear in the central XZ-slices of the reconstructions from WBP and ART1, whereas they are eliminated by FIRT20 (Fig. 5A). Only the reconstruction from FIRT20 (Fig. 5A) yields a 90° re-projection with abundant details close to the ground truth (Fig. 4A).

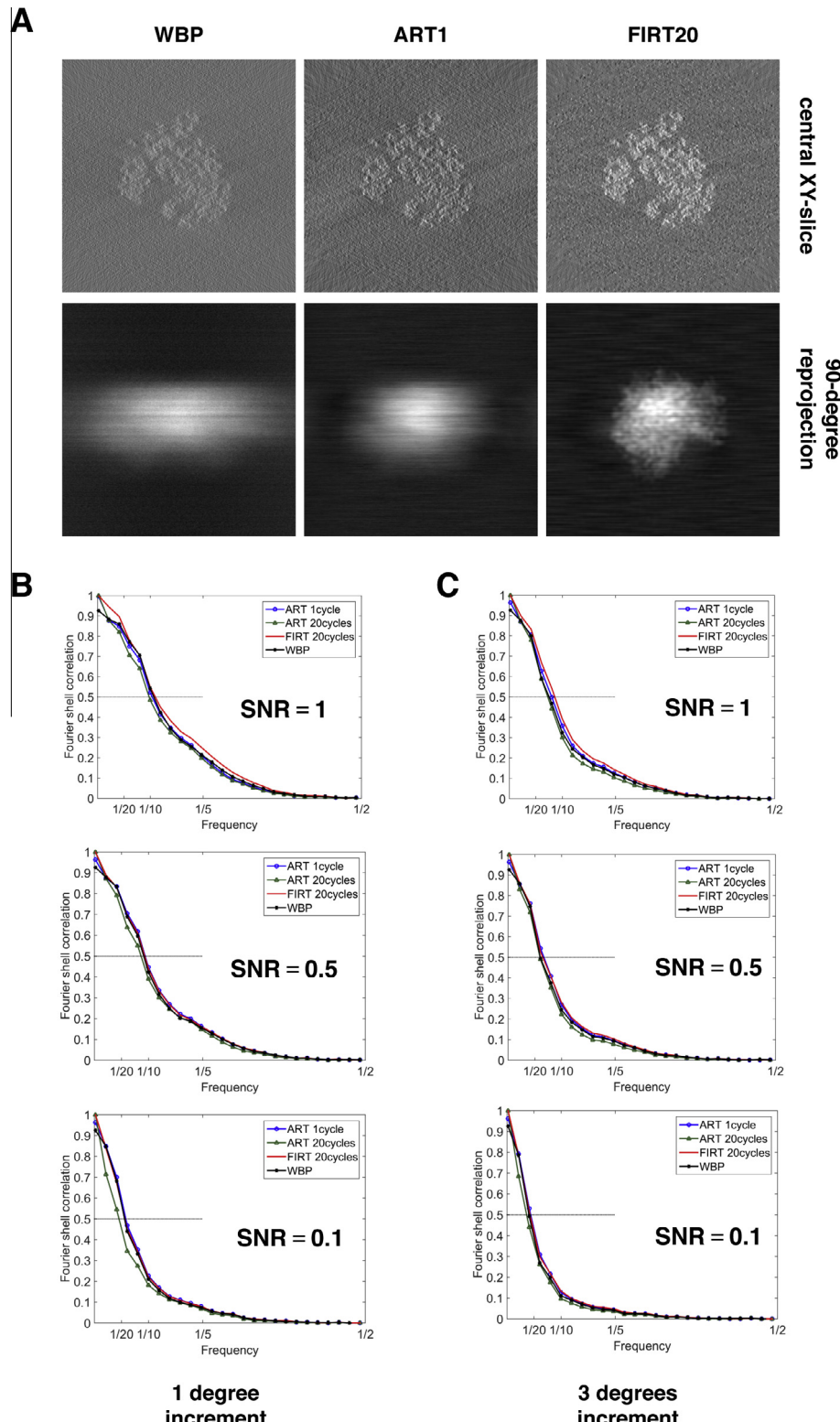


**Fig. 5.** The FIRT reconstruction of simulated datasets with Gaussian noise (SNR = 1, 0.5 and 0.1) and angle step 1° and 3°. (A) The central XZ-slices of the reconstructions of the SNR = 1 simulated dataset with the angular increment of 1° by WBP, ART1 and FIRT20, respectively (upper) and the 90° re-projections of the corresponding reconstructions (lower). (B) and (C) The FSC curves between the reconstructions and the ground truth for different SNRs and angular increments.

By investigating the FSC curves between the reconstructed maps and the ground truth, we also found that, for the simulated data set with an SNR of 1, the FIRT can always reconstruct an improved map that is closer to the ground truth (Fig. 5B and C). However, for the simulated data sets with SNRs of 0.5 and 0.1, the improvement is not obvious according to the FSC curves (Fig. 5B and C). When the SNR becomes lower, the improvement by the FIRT becomes less significant, indicating the limitation of the FIRT in highly noisy data sets. It should be noted that the FSC curve for ART20 was also generated as a control to confirm that the improvement by FIRT20 is actually due to the introduction of ND into the ART iteration (Fig. 5B and C).

In summary, for the simulated noisy data sets, the FIRT can also generate improved reconstructions by reducing ray artifacts and restoring missing information at the non-sampled angular regions.

### 3.4. Testing the FIRT by using the negatively stained protein data set

The pre-aligned tilt series with angle increments of 1° and 3° of negatively stained COPI electron micrographs were reconstructed by WBP, ART2, and FIRT20 (Fig. 6). Here, we utilized two iteration cycles for ART reconstruction to obtain the optimum results and avoid over-fitting of the noise.

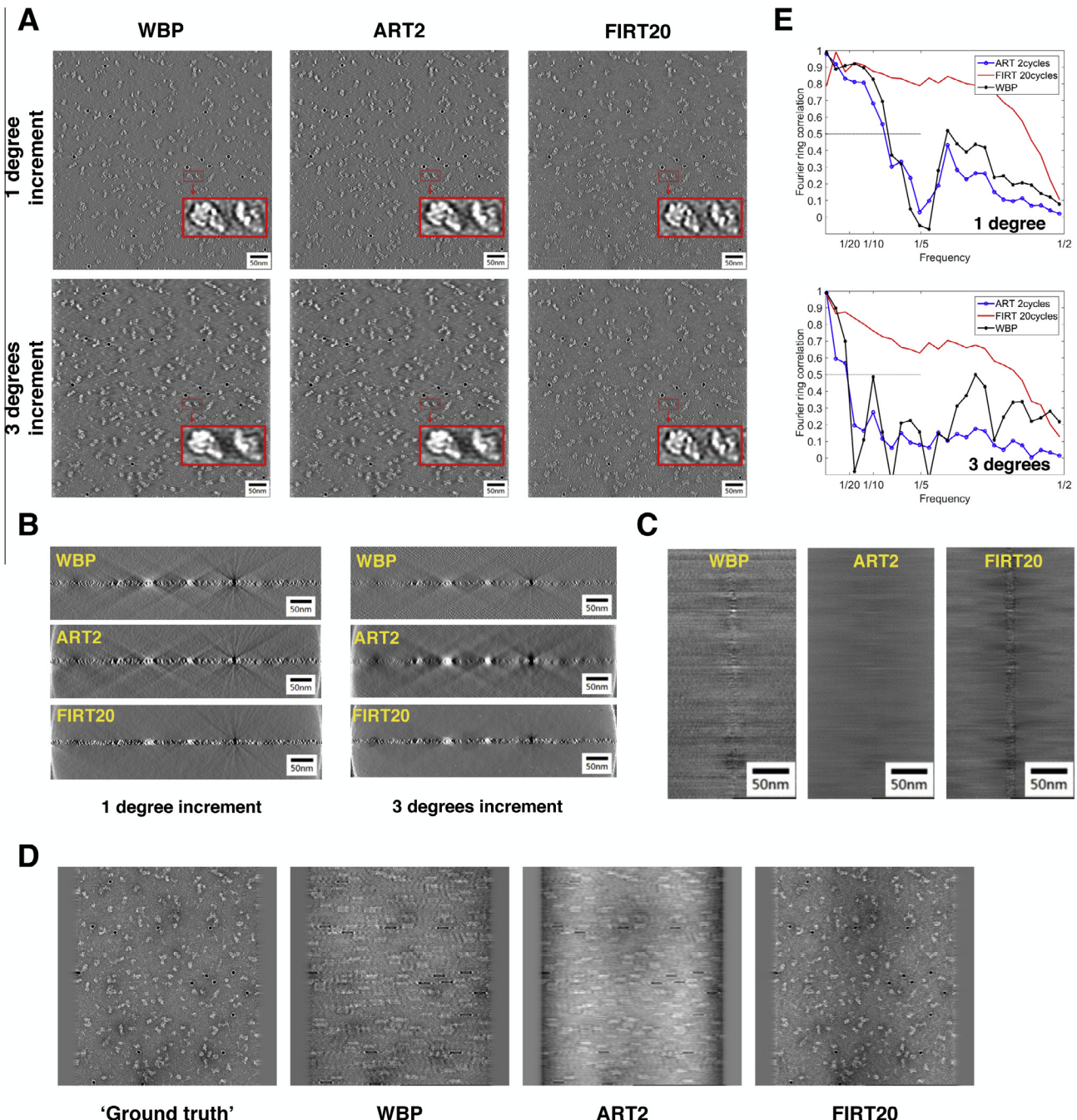


**Fig. 6.** The FIRT reconstruction and cross validation of experimental tomographic dataset for a negatively stained protein COPI with angle step 1° and 3°. (A) The central XY-slices of the reconstructions by WBP, ART2 and FIRT20, respectively. The zoomed particles are shown in the inset. (B) The central XZ-slices of the corresponding reconstructions. (C) The 90° re-projections of the corresponding reconstructions. (D) The excluded projection (omit-projection) at the tilt angle of 0.46° and the 0.46° re-projections of the omit-tomograms for the dataset with the angle step 3°. (E) The cross validation FRC curves between the omit-projection and the corresponding 0.46° re-projections. To be noted, the edges of all projections are Gaussian-padded to generate the reasonable FRCs.

The overall structures of the central XY-slices of the tomograms as reconstructed by WBP, ART2, and FIRT20 (Fig. 6A) seem similar. The tomogram reconstructed by ART2 shows superior contrast, indicating the enhancement of low-frequency information by the ART. However, most importantly, when we identified the COPI particles from the tomograms and magnified their structures in detail, we found that the particles reconstructed by FIRT20 contain more detailed information with sharper edges in comparison to those reconstructed by WBP and ART2 (Fig. 6A). Thus, the tomogram quality of FIRT20 is visually higher than that of WBP and ART2.

We further investigated the central XZ-slices of the tomograms reconstructed by WBP, ART2, and FIRT20 and found that, in consistency with the foregoing tests on simulated data sets, the ray artifacts are significantly inhibited in the FIRT reconstruction and only the rays from the gold nanoparticles are visible, but are less significant (Fig. 6B).

The 90° re-projections of these tomograms were also calculated for comparison (Fig. 6C). The tomogram reconstructed by ART2 does not show any visible meaningful information. Although we could discriminate the projections of the carbon films from the 90° re-projections of the tomograms reconstructed by both WBP and the FIRT, the re-projection from FIRT reconstruction shows a significantly clear image with sharp edges and detailed information. We could even measure the thickness of the carbon film that was coated by COPI, stains, and gold nanoparticles. Although no ground truth of the re-projection is available for comparison and validation, the physical nature of the specimen itself verifies the effectiveness of the FIRT in reducing ray artifacts and restoring missing information of the specimen.

### 3.5. Cross-validation of the FIRT for the negatively stained protein data set

Because no ground truth is available for experimental data, we required another approach to quantitatively validate the information recovered by the FIRT. Here, we used cross-validation to verify the recovered information. We excluded one projection (called omit-projection) from the tilt series and ran the FIRT iteration by using the rest of the projections to generate a tomogram (called omit-tomogram). Normally, we selected the omit-projection with the minimum tilt angle because it affords a higher SNR. We then could quantitatively compare the omit-projection and the re-projection of the omit-tomogram at the same tilt angle by calculating their FRC curve. This cross-validation procedure is similar to the previously reported leave-one-out method (Cardone et al., 2005). More details of this cross-validation are described in the Theory and Methods section.

For the pre-aligned tilt series of negatively stained COPI data sets, we selected the projection with an angle of 0.46° (the minimum tilt) as the omit-projection (Fig. 6D) for both data sets with angle increments of 1° and 3°. After alignment using MarkerAuto (Han et al., 2015), the original nominal 0° set during data collection was calibrated to 0.46°. We then reconstructed the omit-tomograms by using WBP, ART2, and FIRT20, and we computed the re-projections of the corresponding omit-tomograms (Fig. 6D for the data set with an angle increment of 3°). Initial visual investigations clearly show that the re-projections of both the WBP and the ART omit-tomograms are blurred and lack detailed information, whereas the re-projection of the FIRT omit-tomogram is clear with a detailed structure and is significantly similar to the omit-projection (the ground truth). Such visual assessments were further verified quantitatively by comparing the FRC curves between the re-projections and the omit-projection (Fig. 6E). The overall FRC curves reconstructed by WBP and the ART are similar, with a stronger correlation at low resolution for WBP. However, only the FRC

curve reconstructed by the FIRT shows a significantly high correlation between the re-projection and the ground truth. In consistency with the preceding test on the simulated data sets, the improvement of the FIRT again becomes more significant for a larger angular increment according to the FRC validation curves (Fig. 6E).

### 3.6. Testing the FIRT by using the plastic section data set

The pre-aligned tilt series of the plastic section of rat liver tissue was reconstructed by WBP, ART2, and FIRT20. By comparing the tomograms reconstructed by WBP, ART2, and FIRT20 with their central XY-slices (Fig. 7A), XZ-slices (Fig. 7B), and 90° re-projections (Fig. 7C) as well as their cross-validation FRC curves (Fig. 7D and E), we again observed the significant superiority of the FIRT according to an improved SNR (Fig. 7A), reduced ray artifacts (Fig. 7B), and partial restoration of missing information at both the missing wedge (Fig. 7C) and the unsampled angular intervals (Fig. 7D and E).

Thus, for the experimental data sets of both the negatively stained protein complexes and the resin-embedded plastic sections, according to the cross-validation assessment, we proved that the FIRT can restore authentic information of the specimen in the non-sampled angular regions and thereby generate an improved reconstruction.

## 4. Discussion

In the present study, we developed a new ET reconstruction algorithm called the FIRT by combining the conventional ART algorithm and the ND filter to yield high-quality tomograms with fewer ray artifacts, a higher SNR, and partial restoration of missing information in the non-sampled angular regions. The ART is used to generate tomograms under the constraints of the experimental data. The ND filter is used to preserve the smoothness and edge information of the tomogram, which constitute prior knowledge of the biological specimen. The quick convergence ability of the ART enables an efficient switch between the ART (experimental data constraint) and the ND filtering (prior knowledge constraint). Thus, the reconstruction results during FIRT iterations can be improved gradually. Tests of simulated data sets without noise and with SNRs of 1, 0.5, and 0.1 as well as the experimental tomographic data sets on a negatively stained specimen and a plastic section sample proved the higher effectiveness of the FIRT algorithm compared to the WBP and ART, which are currently widely used in the field of ET.

To verify the information restored by the FIRT on the basis of experimental data, we used a cross-validation method that involves extracting the omit-projection and calculating the omit-tomogram. The quick drop of the FRC curves between the omit-projection and the re-projection of the omit-tomogram for the WBP method and ART showed that only low-resolution information in the non-sampled region is reliable. However, the significantly improved FRC curve for the FIRT method proved its ability in restoring authentic information of the specimen in the non-sampled regions.

This cross-validation method can also be used to determine the convergence of the FIRT iteration as described in the FIRT workflow. The convergence of the PCC is actually not an effective criterion owing to the severe over-fitting of noise, which has been demonstrated here by investigating the convergence behavior of the ART. The FRC between the omit-projection and the re-projection of the omit-tomogram reflects the correlation only between signals, because the noise cannot be restored. Thus, the convergence of the FRC is an efficient intimation of the convergence of the FIRT iteration. In practical applications, this method can be used to monitor the iteration convergence and determine the correct number of

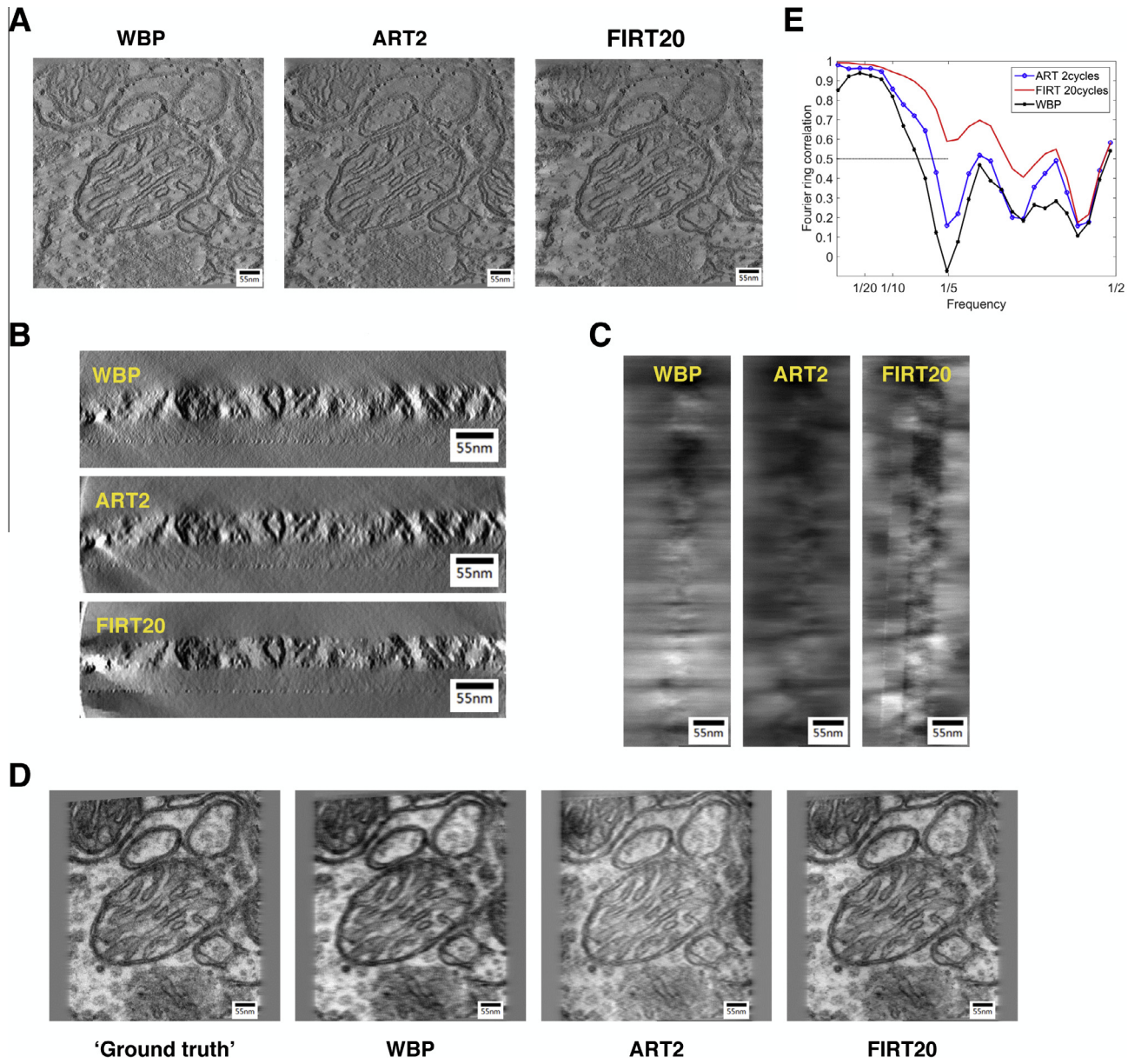


**Fig. 7.** The FIRT reconstruction and cross validation of experimental tomographic dataset for a plastic section specimen. (A) The central XY-slices of the reconstructions by WBP, ART2 and FIRT20, respectively. (B) The central XZ-slices of the corresponding reconstructions. (C) The 90° re-projections of the corresponding reconstructions. (D) The omit-projection at the tilt angle of 0.12° and the 0.12° re-projections of the omit-tomograms. (E) The cross validation FRC curves between the omit-projection and the re-projections. To be noted, the edges of all projections are Gaussian-padded to generate the reasonable FRCs.

iterations for FIRT reconstructions. In addition, the FRC cross-validation curve measures the faithfulness of the restored information compared with the ground truth, and thus, a filtering mask in the Fourier domain can be generated according to an FRC of 0.5 and be used to remove unreliable restored information. This masking procedure is crucial to the superiority of FIRT. In future work, the FRC curve can be adjusted by considering the effect of noise compensation according to a previous study (Cardone et al., 2005).

Although the advantages of the FIRT were proved for both the simulated and the experimental data sets, we also observed its possible limitations in a test on a simulated noisy data set. When the SNR of the data set decreases, the effectiveness of the FIRT decreases gradually. This is probably because the prior knowledge restriction of ND filtering does not function properly for data with a high noise level or because we did not find the correct

parameters for ND filtering in Eq. (1). We attempted to test the FIRT by using some cryo-ET data sets with low SNRs. The quality of the final reconstruction was not significantly improved in comparison to that of WBP. This is presumably because the priori condition of the specimen smoothness becomes less valid for very noisy data sets. Therefore, data with high noise levels must be studied in the future work.

Missing information has long been a problem in the field of ET. This problem causes many difficulties in subsequent image processing steps such as sub-volume averaging and the interpretation of biological structures. Although many methods have been proposed for solving this problem, the FIRT provides a new and simple approach to improve the reconstruction quality with significant restoration of missing information. This should greatly benefit single-particle tomography studies in the future.

## Authors' contributions

The project was initiated by KZ and promoted by FS. FS and FZ supervised the project. KZ designed the original algorithm and wrote the initial codes. YC, YZ and YD improved the algorithm by introducing cross validation and verification mask, which is important for experimental data. YC implemented the final codes. YC and YZ performed experiments. SW performed sample preparation and image collection for negatively stained experimental data. YC prepared figures. YZ, YC and FS wrote the manuscript.

## Competing financial interests

The authors declare no competing financial interests.

## Acknowledgements

We would like to thank Yang Shi and Danyang Zhang (F.S. lab) and Dr. Zhenxi Guo (CBI) for their helps in sample preparation and data collection, and Yili Chen (an intern student in F.S. lab) and

Prof. Paolo Barbano (Duke University) for their useful discussions at the early stage of this project. We would like also to thank Dr. Kaiyong Zhao (Dà-Jiāng Innovations Science and Technology Co., Ltd.) for his help on GPU programing at the early stage of this project. This work was supported by grants from the Strategic Priority Research Program of Chinese Academy of Sciences (XDB08030202) to F.S. and F.Z., the National Basic Research Program (973 Program) of Ministry of Science and Technology of China (2014CB910700) to F.S., and National Natural Science Foundation of China (61232001, 61472397 and 61502455 to F.Z., 31470037 and 31100617 to Y.Z.). All experimental data were collected at Center for Biological Imaging (CBI, <http://cbi.ibp.ac.cn>). And all the intensive computations were also performed by using the high performance computers at CBI, Institute of Biophysics, Chinese Academy of Sciences.

## Appendix A

We illustrate the details of our implement of ND filter by showing the pseudo C-code.

### Parameter declaration:

**data** – a 2D slice of reconstructed volume

**filteredData** – a 2D slice of filtered data

**width** – the width of the 2D slice

**height** – the height of the 2D slice

**t** – the iteration number, in the present study, **t** = 200

**coef** – the constant coefficient, in the present study, **coef** = 0.2

**K** – the threshold value to control the diffusion intensity, defined by user

```

ksq = K * K;
for (ti = 0 ; ti < t ; ti++){
    for (j = 0; j < height; j++){
        jp1 = j == height -1 ? height -1 : j + 1;
        jm1 = j == 0 ? 0 : j - 1;
        for (i = 0; i < width; i++){
            ip1 = i == width -1 ? width -1 : i + 1;
            im1 = i == 0 ? 0 : i - 1;
            gradN = diffN = data[jm1* width + i] - data[j* width + i];
            gradS = diffS = data [jp1* width + i] - data [j* width + i];
            gradE = diffE = data [j* width + ip1] - data [j* width + i];
            gradW = diffW = data [j* width + im1] - data [j* width + i];
            cN = 1.0 / (1.0 + gradN * gradN / ksq);
            cS = 1.0 / (1.0 + gradS * gradS / ksq);
            cE = 1.0 / (1.0 + gradE * gradE / ksq);
            cW = 1.0 / (1.0 + gradW * gradW / ksq);
        }
        filteredData[j* width + i] = data [j* width + i] + coef*(cN*diffN + cS*diffS + cE*diffE + cW*diffW);
    }
    memcpy(data,filteredData,width*height*sizeof(float));
}

```

## Appendix B

We illustrate the details of the weight matrix W and our implementation of ART by showing the pseudo C-code of the re-projection step.

---

### Parameter declaration:

**data** – a 2D slice of 3D reconstructed volume  
**width** – the width of the 2D slice  
**height** – the height of the 2D slice  
**angle** – the angle of projection rays  
**dist\_from\_center** – the distance between one ray and the ray passes the center of the 2D slice, ranges in {-width/2,-width/2+1,-width/2+2,...0,...width/2-1} and is 0 for the ray passes the center of the 2D slice  
**rate** – the sampling step along the projection ray measured in pixel  
**one\_calc\_gray** – the value of the re-projection ray needs to be calculated

---

```

sin_thita = sin(angle);
cos_thita = cos(angle);
//*****Calculate the start point and end point of the re-projection ray
Lter_LZstart = 0.0;
Lter_LZend = height;
Lter_LXstart = (dist_from_center + (Lter_LZstart - height/2.0)*sin_thita)/cos_thita + width/2.0;
Lter_LXend = (dist_from_center + (Lter_LZend - height/2.0)*sin_thita)/cos_thita + width/2.0;
//*****sampling step along the re-projection ray
rate=0.1;
xstep = rate*sin_thita;
zstep = rate*cos_thita;
//*****initialize value of the re-projection ray
one_calc_gray = 0.0;
//*****Re-projection Step -- calculate one_calc_gray along the path of the ray
xcur = Lter_LXstart;
zcur = Lter_LZstart;
while (zcur < Lter_LZend) {
    if (xcur >= 0.0 && xcur < width) {
        x = (int)(xcur);
        z = (int)(zcur);
        if (x < width - 1) xp1 = x + 1; else xp1 = x;
        if (z < height - 1) zp1 = z + 1; else zp1 = z;
        dx = xcur - (float)x;
        dz = zcur - (float)z;
        //*****dual linear interpolation
        one_calc_gray += data[z*width + x]
            + (data[z*width + xp1] - data[z*width + x])*dx
            + (data[zp1*width + x] - data[z*width + x])*dz
            + (data[zp1*width + xp1] + data[z*width + x] - data[z*width + xp1] - data[zp1*width +
x ])*dx*dz;
    }
    xcur += xstep;
    zcur += zstep;
}
normalizeFactor=height/(rate*rate);
one_calc_gray /= normalizeFactor;

```

---

## Appendix C. Supplementary data

Supplementary data associated with this article can be found, in the online version, at <http://dx.doi.org/10.1016/j.jsb.2016.04.015>.

## References

- Andersen, A.H., Kak, A.C., 1984. Simultaneous Algebraic Reconstruction Technique (SART): A superior implementation of the ART algorithm. *Ultrason. Imaging* 6, 81–94.
- Arslan, I., Tong, J.R., Midgley, P.A., 2006. Reducing the missing wedge: high-resolution dual axis tomography of inorganic materials. *Ultramicroscopy* 106, 994–1000.
- Asano, S., Fukuda, Y., Beck, F., Aufderheide, A., Forster, F., Danev, R., Baumeister, W., 2015. Proteasomes, a molecular census of 26S proteasomes in intact neurons. *Science* 347, 439–442.
- Cardone, G., Grunewald, K., Steven, A.C., 2005. A resolution criterion for electron tomography based on cross-validation. *J. Struct. Biol.* 151, 117–129.
- Castano-Diez, D., Kudryashev, M., Arheit, M., Stahlberg, H., 2012. Dynamo: a flexible, user-friendly development tool for subtomogram averaging of cryo-EM data in high-performance computing environments. *J. Struct. Biol.* 178, 139–151.
- Engel, B.D., Schaffer, M., Albert, S., Asano, S., Plitzko, J.M., Baumeister, W., 2015. In situ structural analysis of Golgi intracisternal protein arrays. *Proc. Natl. Acad. Sci. U.S.A.* 112, 11264–11269.
- Frangakis, A.S., Hegerl, R., 2001. Noise reduction in electron tomographic reconstructions using nonlinear anisotropic diffusion. *J. Struct. Biol.* 135, 239–250.
- Frank, J., 2006. Three-dimensional Electron Microscopy of Macromolecular Assemblies, 27.
- Fridman, K., Mader, A., Zwerger, M., Elia, N., Medalia, O., 2012. Advances in tomography: probing the molecular architecture of cells. *Nat. Rev. Mol. Cell Biol.* 13, 736–742.
- Gilbert, P., 1972. Iterative methods for the three-dimensional reconstruction of an object from projections. *J. Theor. Biol.* 1972, 13.
- Gordon, R., Bender, R., Herman, G.T., 1970. Algebraic reconstruction techniques (ART) for three-dimensional electron microscopy and X-ray photography. *J. Theor. Biol.* 29, 471–481.
- Goris, B., Broek, W.V.d., Batenburg, K.J., Mezherji, H.H., Bals, S., 2012. Electron tomography based on a total variation minimization reconstruction technique. *Ultramicroscopy* 113, 120–130.
- Han, R., Wang, L., Liu, Z., Sun, F., Zhang, F., 2015. A novel fully automatic scheme for fiducial marker-based alignment in electron tomography. *J. Struct. Biol.* 192, 403–417.
- Han, R., Zhang, F., Wan, X., Fernandez, J.J., Sun, F., Liu, Z., 2014. A marker-free automatic alignment method based on scale-invariant features. *J. Struct. Biol.* 186, 167–180.
- Kak, A.C., Slaney, M., 1989. Principles of Computerized Tomographic Imaging. I.E.E. E. Press.
- Kremer, J.R., Mastronarde, D.N., McIntosh, J.R., 1996. Computer visualization of three-dimensional image data using IMOD. *J. Struct. Biol.* 116, 71–76.
- Lanzavecchia, S., Cantele, F., Bellon, P.L., Zampighi, L., Kreman, M., Wright, E., Zampighi, G.A., 2005. Conical tomography of freeze-fracture replicas: a method for the study of integral membrane proteins inserted in phospholipid bilayers. *J. Struct. Biol.* 149, 87–98.
- Leary, R., Saghi, Z., Midgley, P.A., Holland, D.J., 2013. Compressed sensing electron tomography. *Ultramicroscopy* 131, 70–91.
- Lucic, V., Rigort, A., Baumeister, W., 2013. Cryo-electron tomography: the challenge of doing structural biology in situ. *J. Cell Biol.* 202, 407–419.
- Ludtke, S.J., Baldwin, P.R., Chiu, W., 1999. EMAN: semiautomated software for high-resolution single-particle reconstructions. *J. Struct. Biol.* 128, 82–97.
- Mastronarde, D.N., 1997. Dual-axis tomography: an approach with alignment methods that preserve resolution. *J. Struct. Biol.* 120, 343–352.
- Orlova, E.V., Saibil, H.R., 2011. Structural analysis of macromolecular assemblies by electron microscopy. *Chem. Rev.* 111, 7710–7748.
- Paaolainen, L., Acar, E., Tuna, U., Peltonen, S., Moriya, T., Soonsawad, P., 2014. Compensation of missing wedge effects with sequential statistical reconstruction in electron tomography. *PLoS ONE* 9, 1–14.
- Perona, P., Malik, J., 1990. Scale-Space and Edge-Detection Using Anisotropic Diffusion. *IEEE Trans. Pattern Anal.* 12, 629–639.
- Radermacher, M., 1992. Electron Tomography, Chapter 5: Weighted Back-Projection.
- Rigort, A., Villa, E., Bäuerlein, F.J.B., Engel, B.D., Plitzko Jr., M., 2012. Integrative approaches for cellular cryo-electron tomography: correlative imaging and focused ion beam micromachining. In: Thomas, M.I.-R., Paul, V. (Eds.), *Methods in Cell Biology*. Academic Press, pp. 259–281 (Chapter 14).
- Sahiner, B., Yagle, A.E., 1993. A fast algorithm for back projection with linear interpolation. *IEEE Trans. Image Process.* 2, 547–550.
- Schekman, R., Orci, L., 1996. Coat proteins and vesicle budding. *Science* 271, 1526–1533.
- Scheres, S.H.W., 2012a. A Bayesian view on Cryo-EM structure determination. *J. Mol. Biol.* 415, 13.
- Scheres, S.H.W., 2012b. RELION: implementation of a Bayesian approach to cryo-EM structure determination. *J. Struct. Biol.* 180, 12.
- Schur, F.K., Hagen, W.J., Rumlova, M., Ruml, T., Muller, B., Krausslich, H.G., Briggs, J. A., 2015. Structure of the immature HIV-1 capsid in intact virus particles at 8.8 Å resolution. *Nature* 517, 505–508.
- Song, K., Comolli, L.R., Horowitz, M., 2012. Removing high contrast artifacts via digital inpainting in cryo-electron tomography: an application of compressed sensing. *J. Struct. Biol.* 178, 108–120.
- Taylor, D.J., Devkota, B., Huang, A.D., Topf, M., Narayanan, E., Sali, A., Harvey, S.C., Frank, J., 2009. Comprehensive molecular structure of the eukaryotic ribosome. *Structure* 17, 1591–1604.
- Wan, X., Zhang, F., Chu, Q., Zhang, K., Sun, F., Yuan, B., Liu, Z., 2011. Three-dimensional reconstruction using an adaptive simultaneous algebraic reconstruction technique in electron tomography. *J. Struct. Biol.* 175, 277–287.
- Weickert, J., 1998. Anisotropic Diffusion in Image Processing.
- Yahav, T., Maimon, T., Grossman, E., Dahan, I., Medalia, O., 2011. Cryo-electron tomography: gaining insight into cellular processes by structural approaches. *Curr. Opin. Struct. Biol.* 21, 670–677.
- Zampighi, G.A., Zampighi, L., Fain, N., Wright, E.M., Cantele, F., Lanzavecchia, S., 2005. Conical tomography II: a method for the study of cellular organelles in thin sections. *J. Struct. Biol.* 151, 263–274.